J. Fluid Mech. (1985), *vol.* 156, *pp.* 237–256
Printed in Great Britain

Measurements of local skin friction in a microbubble-modified turbulent boundary layer

By N. K. MADAVAN, S. DEUTSCH AND C. L. MERKLE

The Department of Mechanical Engineering and the Applied Research Laboratory, The Pennsylvania State University, University Park, PA 16802

(Received 4 September 1984)

Local skin-friction reductions have been measured using an array of flush-mounted hot-film probes in a microbubble-modified, zero-pressure-gradient, turbulent boundary layer. The results of earlier integrated skin-friction measurements, that showed the reduction to be a function of plate orientation, gas-flow rate and free-stream velocity, have been confirmed both qualitatively and quantitatively. With the measurement plate oriented so that buoyancy keeps the bubbles in boundary layer, it is shown that skin friction is reduced monotonically for all air-flow rates at each of three free-stream velocities between 4 and 17 m/s. For the opposite plate orientation it is possible for increasing gas injection to lead to smaller local skin-friction reduction at the lowest speeds. Drag reduction appears to persist for as much as 60–70 boundary-layer thicknesses downstream of the injection region. It is further shown, using a probe flush-mounted just upstream of the injection section, that there is no apparent upstream interference due to the gas injection. Spectral measurements indicate that microbubbles can cause a reduction of high-frequency shear-stress fluctuations. This suggests a destruction of some of the turbulence in the near-wall region.

1. Introduction

The authors (Madavan, Deutsch & Merkle 1984*a*,*b*; hereinafter referred to as MDM1 and MDM2) have recently shown that the introduction of gas bubbles (microbubbles) into a hydrodynamic turbulent boundary layer results in significant reductions in skin friction. In a series of experiments building on some earlier Soviet work (Migirenko & Evseev 1974; Bogdevich & Malyuga 1976; Bogdevich & Evseev 1976), integrated skin-friction measurements were made on a 102×254 mm force balance downstream of a porous injection section. Microbubbles were introduced into the boundary layer by injecting gas (usually air) through the porous surface. The effect of buoyancy, gas flow rate, freestream velocity, gravitational orientation and porous material on the integrated skin-friction reduction have been documented in MDM1 and MDM2. Generally speaking, the measurements have shown that the magnitude of the skin-friction reduction increases with air flow rate and that it is the ratio of the volumetric flow rate of gas to that of water that is the important parameter. Tests with various types of porous surfaces, including pore-size variations over a range of 0.5–100 μm, have shown that the skin-friction reduction can be realized with a variety of porous materials, although details of the variation of the skin-friction reduction with air flow rate are slightly dependent on the type of material.

The microbubble-laden turbulent boundary layer is an extremely complicated flow field and the mechanisms which lead to the observed skin-friction reductions remain unclear. Certainly a proper understanding of the phenomenon cannot be expected from integrated skin-friction measurements alone and calls for the measurement of additional details of the flow field. A more precise knowledge of the microbubble volumetric-concentration profiles and bubble size distributions, as well as the modified mean-velocity profiles and corresponding turbulence characteristics, are necessary prerequisites for achieving such understanding. This information, however, is very difficult to obtain. First, it is noted that the bubble concentrations of interest are quite high (Migirenko & Evseev 1974 have reported peak concentrations as high as 50–80% by volume) so that the microbubble-laden boundary layer is optically opaque, thus precluding the use of contemporary optical measurement techniques. Secondly, both the earlier reported gravitational effects (MDM1, MDM2) and simple models of the bubble formation process suggest the phenomenon is operative only at high unit Reynold numbers. Thus, the boundary layers of interest are extremely thin, further hampering measurement attempts (boundary layer thicknesses are less than 10 mm, while sublayer thicknesses are a few tens of micrometres in the current experiments).

Measurements of bubble-concentration profiles reported by Migirenko & Evseev (1974), as well as the authors' own results (MDM1), suggest a bubble-free layer very close to the wall. Local skin-friction measurements using flush-mounted hot-film probes become then a practical and attractive first step toward understanding the local characteristics of the microbubble boundary layer. In the current study, an array of flush-mounted hot-film probes has been used to investigate the downstream evolution and persistence of the skin-friction reduction. The instantaneous signals from the hot films have also been utilized to compare the spectral content of the turbulence in the presence and absence of microbubbles.

2. Experimental details

2.1. *Facility and setup*

The experiments were conducted in the rectangular test section of the water-tunnel facility at The Pennsylvania State University using the boundary layer on the tunnel test-section wall. The tunnel is a closed-circuit system and the rectangular test section has dimensions of $508 \times 714 \times 762$ mm long. The flat plate on which the measurements were performed was designed to replace an existing 279×533 mm test-section window. A 102×178 mm porous section for gas injection, followed by a 102×254 mm force balance was centred spanwise on this test plate (see figure 1). Details of the facility used and the experimental setup can be found in MDM1.

An array of six hot-film probes (TSI 1471W) were employed; five of these were flush-mounted on the force balance downstream of the injection section, while the sixth probe was mounted immediately upstream. The locations of the probes are shown schematically on figure 2. The probes were connected to constant-temperature anemometers (both DISA 44MO1 and TSI 1750 sets were used). Normally, the probes were operated at an overheat ratio of 1.06, this value being chosen as a compromise between probe sensitivity and probe life.

The porous material used for air injection was of sintered stainless steel, commercially available for use as filter material. Experiments were conducted with the smallest available filter material (0.5 μm), as well as with a larger size (100 μm). The numbers in parentheses refer to the largest particle size that can pass through the filter, not the actual pore size.

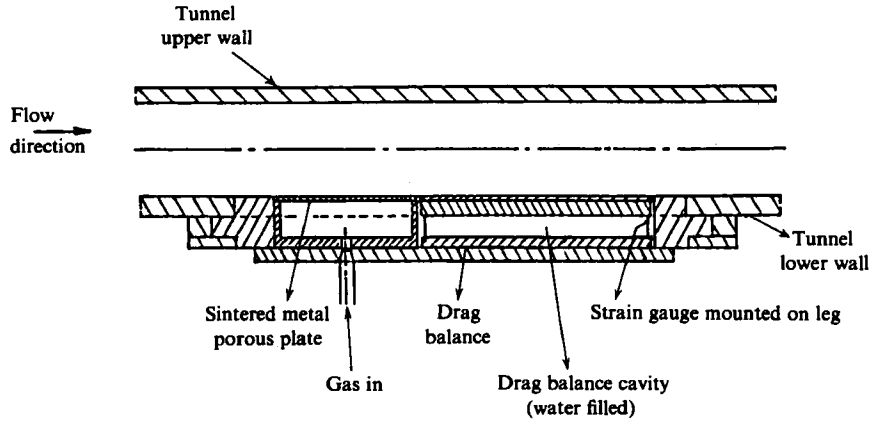

FIGURE 1. Schematic of the experimental setup.

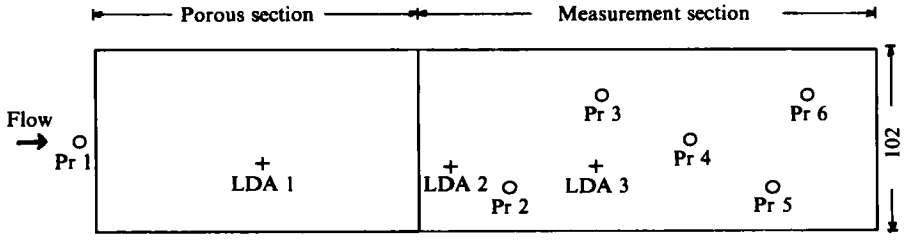

	Distance to virtual origin mm	Distance to leading edge of porous section, mm
Pr 1	170	−10
Pr 2	409	229
Pr 3	460	280
Pr 4	511	331
Pr 5	555	375
Pr 6	575	395
LDA 1	272	92
LDA 2	374	194
LDA 3	454	274

FIGURE 2. Schematic showing hot-film-probe locations and LDA measurement stations. Pr denotes flush mounted hot-film-probe location; LDA denotes LDA measurement station.

The tunnel test-section velocity was monitored by a transducer that measured the pressure drop across the tunnel contraction section. Injected air flow rate and pressure were measured using a flow meter and a pressure transducer.

2.2. *Data acquisition and run procedure*

Two methods of data acquisition were used. In the initial experiments, the signals from the six hot films were recorded on three Nicolet digital oscilloscopes and stored on floppy discs. The storage capacity of the discs limited these measurements to 2048 points. These digitized signals were then transferred to an IBM 4341 mainframe system for reduction and analysis. Other flow parameters, namely tunnel freestream velocity, injected-air flow rate and pressure, were taken manually from digital voltmeter readouts at the instant the hot-film signals were recorded. In the latter stages of the experiments, an analog-to-digital (A/D) converter was used to digitize

the hot-film signals and feed the data directly to an on-line VAX 11/780 computer. Here, the allowable sample size was much larger. For both methods of data acquisition the sampling rate was typically chosen as 2000 Hz. The minimum record length used was about 1 s. In both procedures, the data channels were sampled sequentially, the maximum delay between the first and last channel sampled being about 10 μs. The instantaneous voltages from the films were recorded and linearization was accomplished on the computer.

The run procedure used for the local skin-friction measurements reported here was as follows. The tunnel velocity was held constant and the air flow rate was set at levels ranging from zero to maximum. At each air-flow setting, the oscilloscopes were simultaneously triggered (or sampling was initiated on the A/D converter) to record the hot-film signals. Other flow parameters were recorded at the same time that the oscilloscopes were triggered. (With the A/D converter, these parameters were also automatically sampled.) Immediately before and after each run with microbubbles, probe-calibration runs were performed by recording the hot-film signals over the range of tunnel velocities in the absence of microbubbles.

2.3. *The experimental boundary layer*

The boundary layer into which microbubbles were introduced was documented by measuring the mean-velocity and turbulence-intensity profiles and streamwise pressure gradient in the tunnel test section. Details can be found in MDM1, but for the sake of completeness and the important role these data play in hot-film-probe calibration, the major results are highlighted here.

Mean-velocity profiles were obtained at three streamwise locations (shown in figure 2) and at two different tunnel speeds (4.7 and 10.6 m/s) using a laser-Doppler anemometer (LDA). These results are presented in wall variables in figure 3, taken from MDM1. The friction velocity used in the figure was evaluated by fitting the near-wall data to Coles (1968) law of the wall. The boundary layer was checked for 'full development' by examining the velocity profiles in outer variables, following Purtell, Klebanoff & Buckley (1981). This is shown in figure 4, also taken from MDM1. Similarity in the profiles is noted at both tunnel speeds. These velocity measurements, along with measurements of the pressure gradient along the tunnel test section (see MDM1), establish the experimental boundary layer as being reasonably close to a classical, fully developed, zero-pressure-gradient, turbulent boundary layer.

The calibration procedure adopted here for the hot films (as discussed below) necessitated establishing a virtual origin for the experimental boundary layer. This was accomplished using the boundary-layer displacement and momentum thicknesses (δ^* and θ), evaluated from the mean-velocity profiles discussed above. Since, for a flat-plate turbulent boundary layer, both δ^* and θ are proportional to the distance from the virtual origin to the 0.8 power ($\frac{4}{5}$), the latter can be linearly extrapolated from a plot of $\delta^{*\frac{4}{5}}$ and $\theta^{\frac{4}{5}}$ versus streamwise distance (referenced to a known location along the boundary layer). By this procedure, the location of the virtual origin was established 180 mm upstream of the porous injection section, as shown in figure 5.

2.4. *Skin-friction probe calibration procedure*

Flush-mounted hot-film probes relate the heat-transfer rate from the film to the fluid shear stress at the wall. For constant-temperature operation of the film, this relationship between the instantaneous voltage output by the anemometer E (which is directly related to the electrical heat dissipated by the film), and the instantaneous *shear stress* τ_w is of the form

$$\tau_w^{\frac{1}{3}} = AE^2 + B. \tag{1}$$

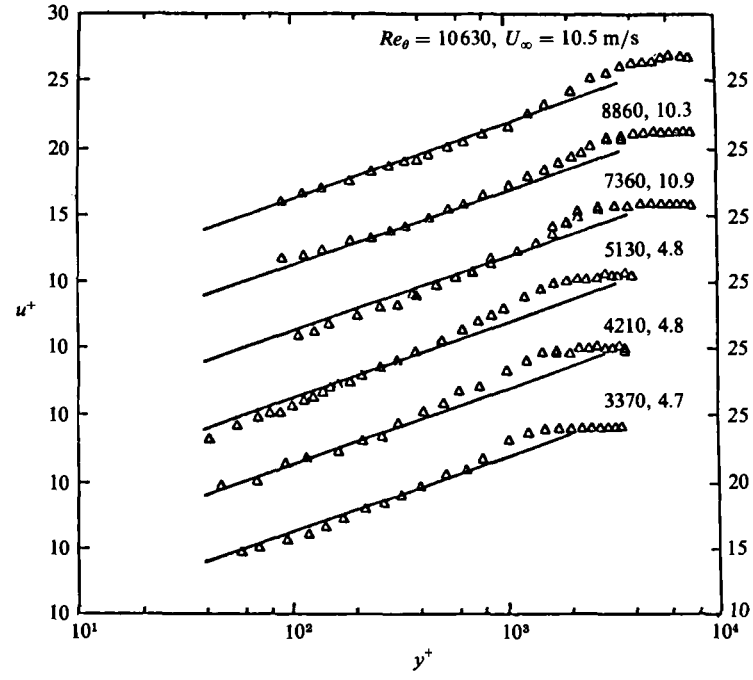

FIGURE 3. LDA velocity-profile measurements in the undisturbed boundary layer presented in inner variables [note shifted origins]. The solid lines are $u^+ = 5.62 \log y^+ + 5.0$.

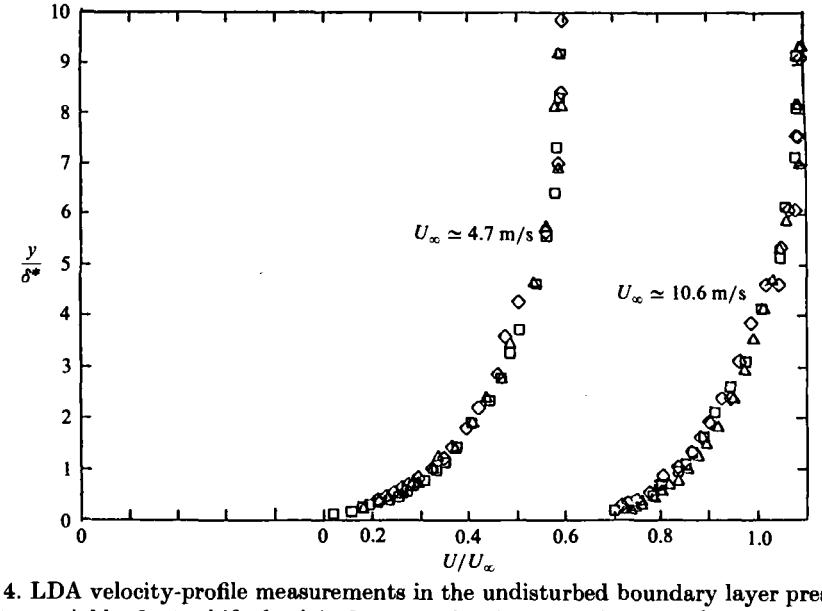

FIGURE 4. LDA velocity-profile measurements in the undisturbed boundary layer presented in outer variables [note shifted origins]: ◇, station 1; △, station 2; and, □, station 3.

Here A and B are constants that must be determined by a calibration procedure in a flow where the shear stress is known either from theory or an independent measurement. Brown (1967), Liepmann & Skinner (1954), and others have suggested that the constants, A and B, determined from a calibration in a laminar flow can be used for measurement in a turbulent flow. The validity of such a procedure has,

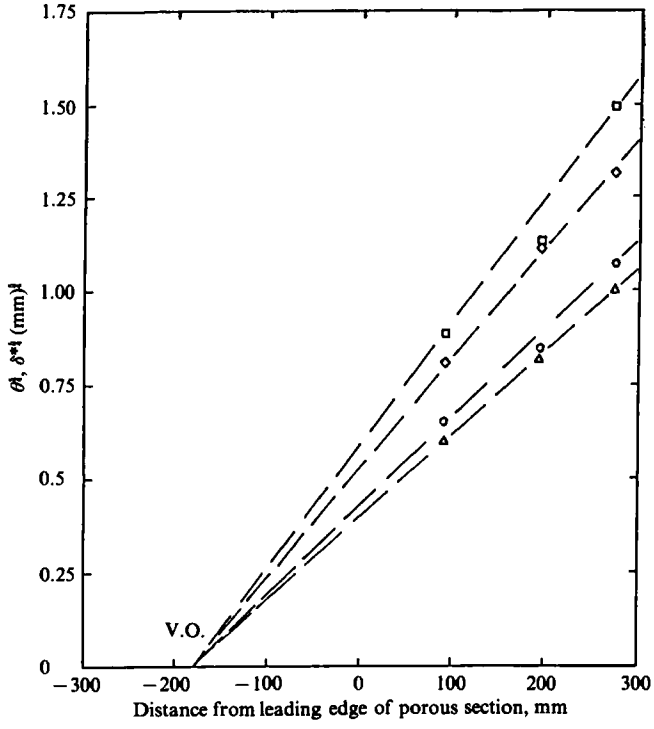

FIGURE 5. Determination of the virtual origin: □, δ^* values, $U_\infty = 4.7$ m/s; ◇, δ^* values, $U_\infty = 10.6$ m/s; ○, θ values, $U_\infty = 4.7$ m/s; △, θ values, $U_\infty = 10.6$ m/s.

however, been questioned (see, for example, Bellhouse & Schultz 1966; Bradshaw & Gregory 1961), since the response of the hot film in a turbulent flow is not necessarily identical to that in a laminar flow with the same shear stress. Moreover, it is difficult to obtain a laminar flow for the calibration experiment, especially one that can cover the range of shear-stress values expected in an actual turbulent-flow application (Ramaprian & Tu 1983). This is particularly true for the high unit Reynolds number boundary layers of interest here.

In the present study, an *in situ* calibration procedure based upon the verified characteristics of the flat-plate turbulent boundary layer was used. This was accomplished by recording the voltage signals from each probe at a series of different tunnel free-stream velocities in the absence of microbubbles. Each signal record was digitized and stored and the time-averaged voltage $\bar{E}$ was computed. The mean local skin-friction value $\bar{\tau}_w$ at each probe location and each tunnel velocity was then obtained from classical turbulent-boundary-layer correlations of skin friction and length Reynolds number, using the virtual origin established from the LDA measurements of the velocity profiles. The use of the classical correlation is justified by the velocity-profile measurements that indicate the present boundary layer is a zero-pressure-gradient turbulent boundary layer. The specific correlation used was the one suggested by White (1974),

$$\bar{\tau}_w = \frac{1}{2\rho U_\infty^2} \frac{0.455}{\ln^2(0.06 Re_x)}, \tag{2}$$

where ρ is the density of water and Re_x the Reynolds number based on the streamwise length x measured from the virtual origin to the probe location. This correlation is

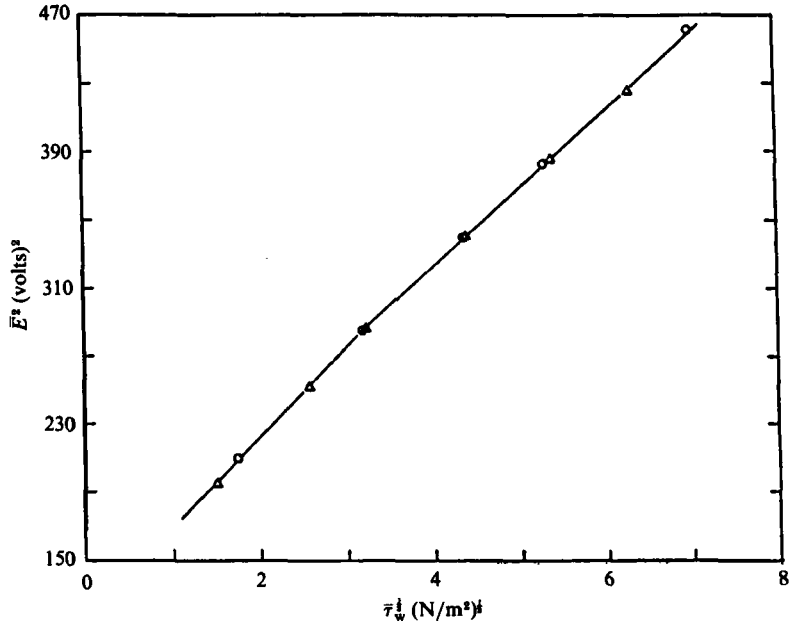

FIGURE 6. A typical calibration curve for the flush-mounted hot-film probes: ○, pre-air-injection calibration; △, post-air-injection calibration; ——, the calibration curve used in the data analysis.

in good agreement with values of $\bar{\tau}_w$ obtained from figure 3. It is worth noting that, at these Reynolds numbers (roughtly 2–10 million), a 10% measurement error in virtual origin will result in no more than a 1% discrepancy in local shear stress.

Having obtained this tabular set of mean voltages and corresponding values of skin friction, the calibration constants A and B in (1) are evaulated by an iterative technique. In this procedure, A and B are initially approximated by fitting (1) to the time-averaged tabular data. These values are then iteratively improved by the method described by Sandborn (1979*a*, *b*) and Hanratty & Campbell (1982). In the present study, one iteration was found to be sufficient. Two calibration curves were fitted to the data, one at low and the other at high velocities. A typical calibration curve is shown in figure 6.

It should be emphasized here that the calibration measurements were made immediately prior to and after measurements with air injection (see figure 6). The average of these two calibrations was used for reducing the hot-film data in the presence of microbubbles. In cases where the pre- and post-calibration showed deviations which resulted in the correlation coefficient of the linear least-squares fit to the data being less than 0.95, the entire data set was discarded.

When there are no bubbles in the boundary layer a measure of the validity of the hot-film technique can be obtained by comparing the r.m.s. intensity of the skin-friction fluctuations τ_w' measured here to those reported in the literature. Mitchell & Hanratty (1966) and Sirkar & Hanratty (1970) report values of $\tau_w'/\bar{\tau}_w$ ranging between 0.32–0.36, obtained from electrochemical shear-stress measurements. Eckelmann's (1974) measurements in the thick viscous sublayer of an oil boundary layer using a flush-mounted hot film provide a value of 0.24. By assuming that very near the wall ($0 \leqslant y^+ \lesssim 0.1$) both the streamwise velocity fluctuations u' and the mean velocity $\bar{U}$ vanish linearly with decreasing distance from the wall,

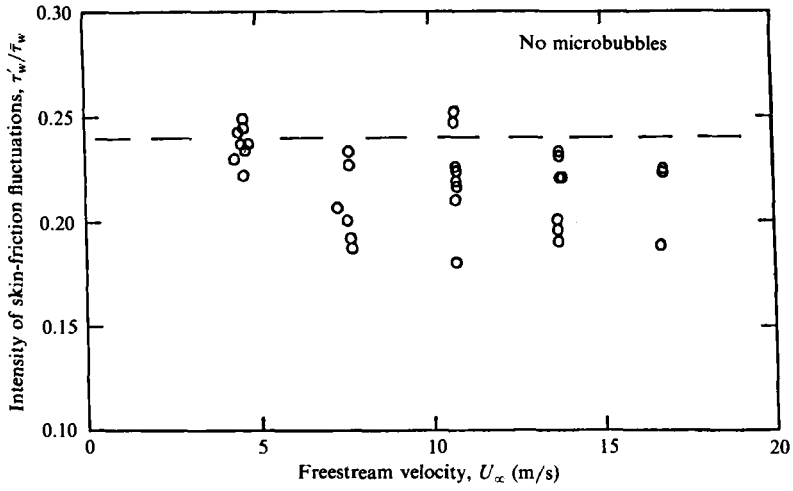

FIGURE 7. Hot-film measurements of the skin-friction fluctuations in the undisturbed boundary layer.

Eckelmann noted that the value of 0.24 was in agreement with the asymptotic slope of Laufer's (1950) measurements of $u'/\bar{U}$.

The measured values of $\tau'/\bar{\tau}_w$ in the absence of microbubbles are compared with the 0.24 value in figure 7 for the tunnel velocity range tested. The data were typically scattered around the value 0.2. The agreement with earlier results seems quite reasonable, particularly when one considers the difficulty in obtaining results at the high unit Reynolds numbers and thin sublayers encountered in this study.

3. Results and discussion

Experiments were conducted at tunnel free-stream velocities ranging between 4 and 17 m/s. For the most part, the porous section fabricated from the smallest available filter material (0.5 μm) was used. Additional experiments were also conducted using the 100 μm porous material. Air flow rates ranged up to 0.006 m^3/s. As is shown later, this flow rate corresponds to a volumetric fraction in the boundary layer of about 0.5, assuming that all of the air flow remains in the boundary layer, which may not be the case.

The local skin-friction measurements with microbubbles reported here are presented in terms of the skin-friction coefficient, C'_f, normalized to the corresponding skin-friction coefficient without microbubbles, C'_{f0}, as a function of the volumetric fraction of air in the boundary layer. The air flow fraction was defined as the volumetric flow rate of air divided by the total flow in the boundary layer,

$$\frac{Q_a}{Q_a+Q_w}, \tag{3}$$

where

$$Q_w \equiv U_\infty(\delta-\delta^*)\,b, \tag{4}$$

and the subscripts a and w denote air and water. The boundary-layer thickness and displacement thickness, δ and δ^*, are obtained from classical correlations (see White 1974). These thicknesses were calculated at the mid-point of the porous section (in the absence of microbubbles). The parameter b is the width of the porous section.

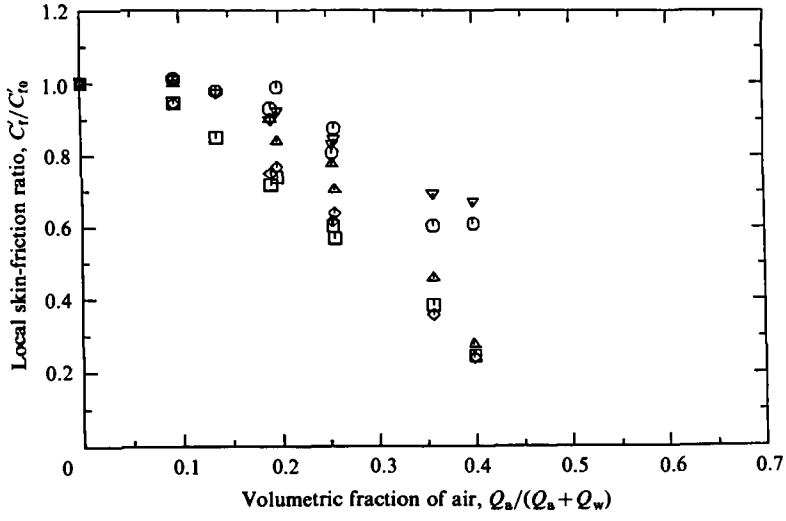

FIGURE 8. Hot-film measurements of the local skin friction with microbubbles as a function of the air flow rate when the plate is below the boundary layer. $U_\infty = 16.7$ m/s (0.5 μm porous section): □, Probe 2; ◇, Probe 3; △, Probe 4; ○, Probe 5; ▽, Probe 6.

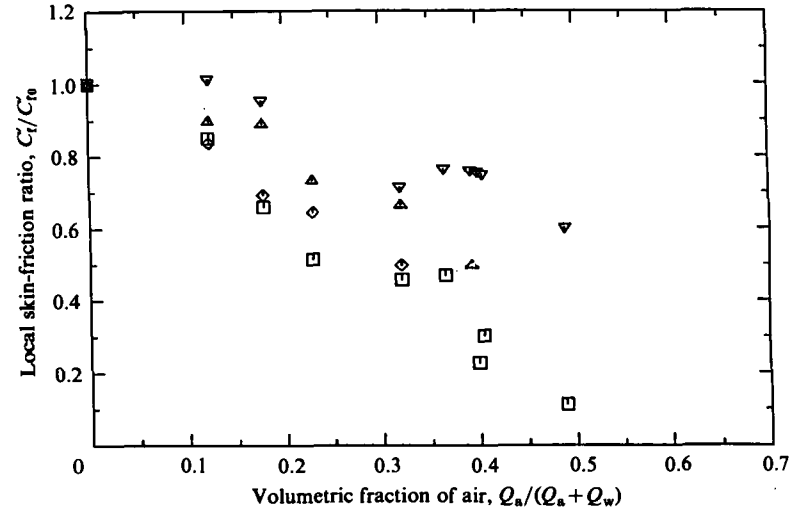

FIGURE 9. Hot-film measurements of the local skin friction with microbubbles as a function of the air flow rate when the plate is below the boundary layer. $U_\infty = 10.8$ m/s (0.5 μm porous section): □, Probe 2; ◇, Probe 3; △, Probe 4; ▽, Probe 6.

3.1. *Plate below the boundary layer*

The local skin-friction measurements at the various hot-film probe locations with the plate below the boundary layer are shown in figures 8–10. Note that this orientation (referred to as plate on bottom on the figures), corresponds to the view shown in figure 1, where the experimental setup is mounted on the bottom wall of the tunnel. The measurements shown in figure 8 are for a tunnel velocity $U_\infty = 16.7$ m/s, while those in figures 9 and 10 correspond to $U_\infty = 10.8$ m/s and $U_\infty = 4.6$ m/s, respectively. The figures represent measurements using the 0.5 μm porous section.

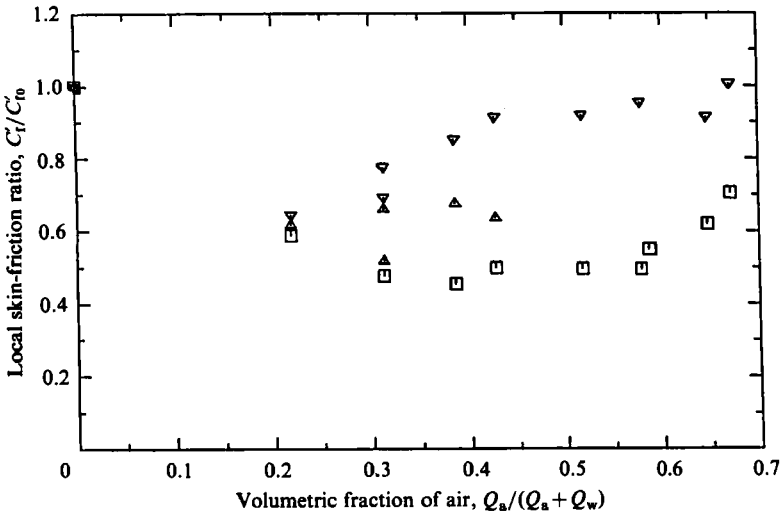

FIGURE 10. Hot-film measurements of the local skin friction with microbubbles as a function of the air flow rate when the plate is below the boundary layer. $U_\infty = 4.6$ m/s (0.5 μm porous section): □, Probe 2; △, Probe 4; ▽, Probe 6.

Skin-friction reductions are noted at all tunnel velocities, but the characteristic trends with volume fraction depend upon U_∞. The reductions are greatest in the region close to the porous section (probes 2 and 3); farther downstream, the skin friction relaxes back toward its undisturbed (no microbubbles) values (probe 6). This is probably due to the decreasing air content in the boundary layer resulting from both boundary-layer growth and bubble migration. At the high and intermediate tunnel velocities (see figures 8 and 9), the decrease in skin friction is seen to be monotonic with increasing air flow except possibly for probes 5 and 6 at low air flows.

In contrast to these high- and intermediate-velocity results, the low-velocity results in figure 10 show that the skin friction goes through a minimum and then increases with increasing air flow. This indicates an optimum air flow rate for maximum skin-friction reduction at low velocities. Based on the results of Silberman (1957) and Hughes, Reischmann & Holzmann (1979) that indicate that the bubble diameter is proportional to the square root of the ratio Q_a/U_∞, one can speculate that the reason for this reduced effectiveness of the bubbles at high air flow rates and low velocities may be due to the larger bubble sizes. These larger bubbles quickly migrate out of the boundary layer with this plate orientation, reducing their effectiveness. The same effect was not observed at the high velocities, apparently because of the shorter convection time.

3.2. *Plate above the boundary layer*

The entire test section of the water tunnel can be rotated through 180°, thus effectively positioning the experimental setup on the upper wall of the tunnel. At this orientation, the plate is above the boundary layer (referred to as plate on top in the figures) and the forces due to gravity act to keep the bubbles in the boundary layer. Earlier reported force-balance measurements (MDM1) showed substantially higher reductions in the integrated skin friction at this orientation, especially at the lower velocities. The hot-film measurements are shown in figures 11–13 and compared to the measurements with the plate below the boundary layer for a range of tunnel

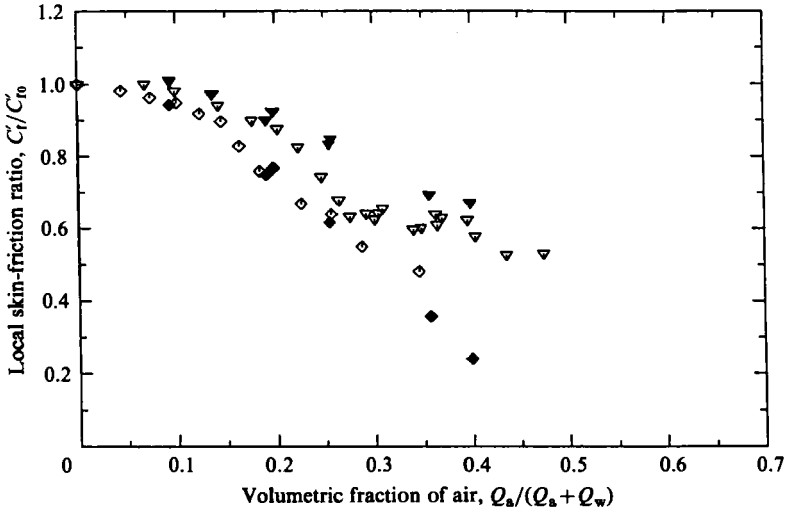

FIGURE 11. The effect of gravity on the hot-film measurements of the local skin friction with microbubbles. Comparison of data taken with the plate above and below the boundary layer. $U_\infty = 16.8$ m/s (0.5 μm porous section). Open symbols are used for plate on top, closed symbols for plate on bottom: ◇, Probe 3; ▽, Probe 6.

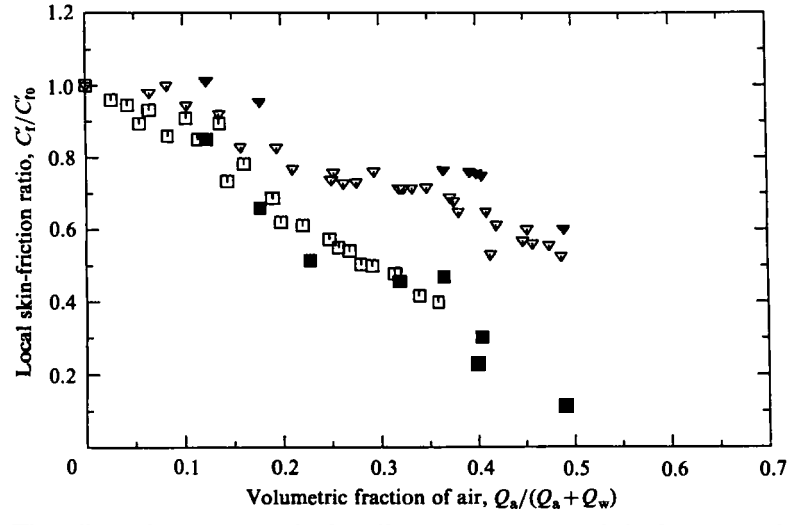

FIGURE 12. The effect of gravity on the hot-film measurements of the local skin friction with microbubbles. Comparison of data taken with the plate above and below the boundary layer. $U_\infty = 10.7$ m/s (0.5 μm porous section). Open symbols are used for plate on top, closed symbols for plate on bottom: □, Probe 2; ▽, Probe 6.

velocities. Figure 11 compares measurements at $U_\infty = 16.8$ m/s for the two plate orientations at probe 3 and probe 6 (note that probe 3 is located close to the injection section and probe 6 is located farthest downstream). While the skin-friction reductions at probe 3 are of the same magnitude, slightly larger reductions are noted at the downstream probe location when the plate is above the boundary layer. Figure 12 is a similar plot at $U_\infty = 10.7$ m/s and compares the measurements for the two orientations at probe 2 and probe 6. Once again, it is noted that, close to the

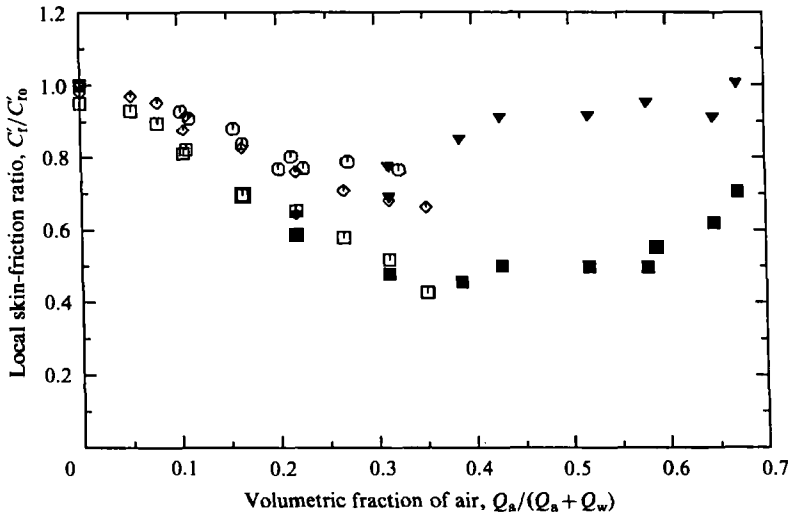

FIGURE 13. The effect of gravity on the hot-film measurements of the local skin friction with microbubbles. Comparison of data taken with the plate above and below the boundary layer. $U_\infty = 4.6$ m/s (0.5 μm porous section). Open symbols are used for plate on top, closed symbols for plate on bottom: □, Probe 2; ◇, Probe 3; ○, Probe 5; ▽, Probe 6.

injection section, the skin-friction reductions are independent of gravitational orientation, while farther downstream the plate-on-top orientation again results in somewhat larger C_f' reductions. These increased reductions with the plate on top occur because the bubbles remain longer in the boundary layer, where they are most effective. Figure 13 presents additional data for a tunnel velocity at 4.6 m/s. Note that data for probe 6 with the plate above the boundary layer are not available. Quantitative comparison between the two orientations in figure 13 is difficult because the maximum air flow rates shown with the plate above the boundary layer are quite small. The fluctuations in the hot-film signals at higher air flow rates were very high and, owing to the resulting lack of confidence in the measurements, these results are not presented. The data, however, suggested that the skin-friction reductions with increasing air flow were monotonic, as compared to the plate-on-bottom orientation where a definite 'bucket' in the curves was noted. These trends seem reasonable when one notes that the maximum integrated skin-friction reductions reported in MDM1 were observed at this velocity ($U_\infty = 4.6$ m/s) with the plate above the boundary layer.

3.3. *Effect of pore-size variations*

The size of the microbubbles is certainly an important parameter in the skin-friction reduction. Although both the Soviet results (Bogdevich & Evseev 1976) and intuition suggest that the pore size would be an important variable, literature (Silberman 1957; Hughes *et al.* 1979) on bubble sizes in turbulent shear flows, though sparse, indicates that the bubble size is not determined primarily by the size of the pores used for injection, but by the characteristics of the flow. To investigate this, two widely different pore sizes, 0.5 and 100 μm, were used for gas injection to compare the magnitude of the skin-friction reductions. Figures 14 and 15 compare measurements made using the 100 and 0.5 μm porous materials for the plate below the boundary layer. Figure 14 compares data at probes 2 and 6 at $U_\infty = 16.8$ m/s. At

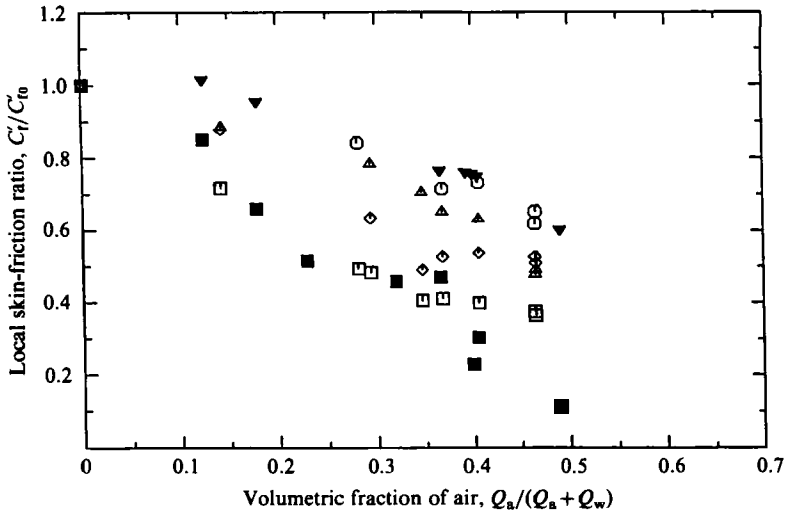

FIGURE 14. The effect of pore-size variations on the local skin-friction measurements. Comparison of data taken with the 0.5 μm and 100 μm porous sections. $U_\infty = 10.7$ m/s. Plate is on the bottom. Open symbols are for the 100 μm porous section, closed symbols for the 0.5 μm porous section: □, Probe 2; ◇, Probe 3; △, Probe 4; ○ Probe 5; ▽, Probe 6.

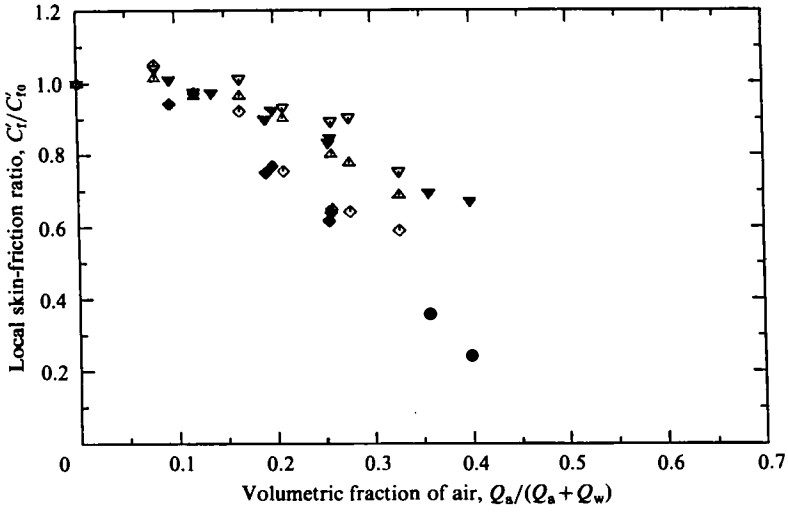

FIGURE 15. The effect of pore-size variations on the local skin-friction measurements. Comparison of data taken with the 0.5 μm and 100 μm porous sections. $U_\infty = 10.7$ m/s. Plate is on the bottom. Open symbols are for the 100 μm porous section, closed symbols for the 0.5 μm section: ◇, Probe 3; △, Probe 4; ▽, Probe 6.

$U_\infty = 10.7$ m/s a direct comparison is not available and, for clarity, figure 15 presents only the results of the closest (probe 2) and the farthest (probe 6) locations for the 0.5 μm porous section (presented earlier in figure 9). These data show that injection pore size does not have a substantial effect on the skin-friction results for the conditions tested here. This observation is in agreement with the integrated skin-friction measurements reported earlier in MDM2. These results are of some practical importance since with the larger-pore-size material much less energy need be expended to introduce a given quantity of microbubbles.

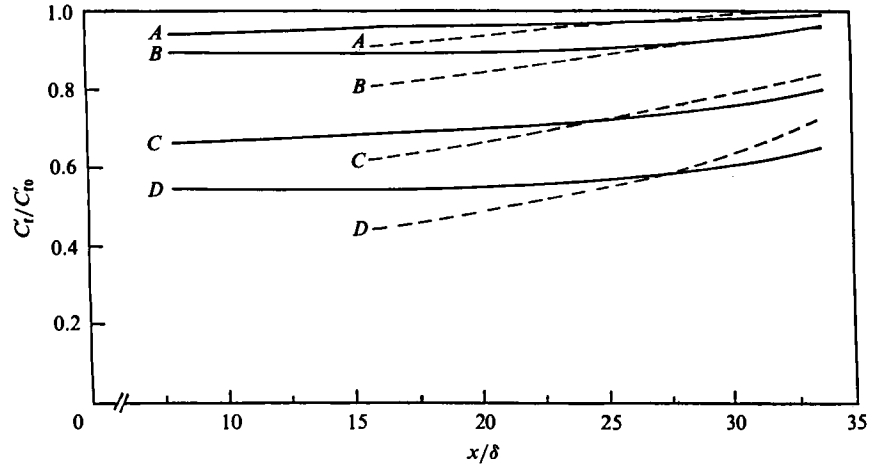

FIGURE 16. The downstream persistence of the skin-friction reduction. Comparison of data taken with the plate above and below the boundary layer. $U_\infty = 16.8$ m/s. The solid line represents the plate on top, the dashed line the plate on bottom. $Q_a/(Q_a+Q_w)$ is 0.13 for A, 0.18 for B, 0.27 for C and 0.34 for D.

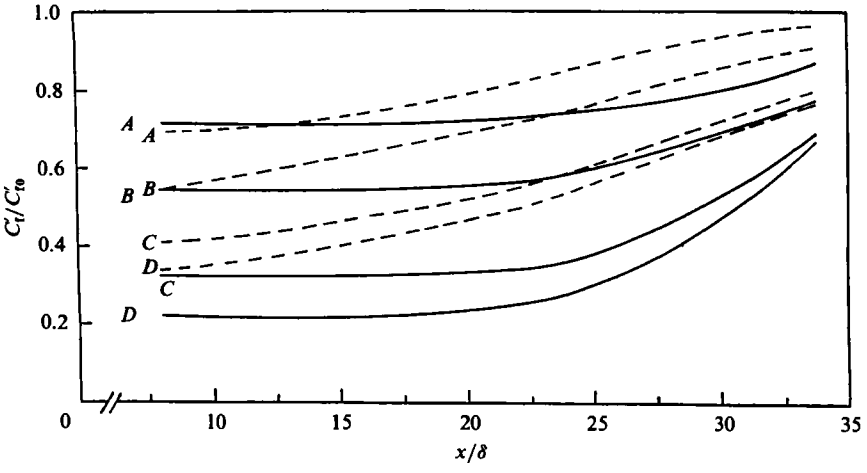

FIGURE 17. The downstream persistence of the skin-friction reduction. Comparison of data taken with the plate above and below the boundary layer. $U_\infty = 10.7$ m/s. The solid line represents the plate on top, the dashed line the plate on bottom. $Q_a/(Q_a+Q_w)$ is 0.17 for A, 0.24 for B, 0.34 for C and 0.39 for D.

3.4. *Persistence of the skin-friction-reduction phenomenon*

The downstream distances to which the skin-friction reductions persist was studied by cross-plotting the data reported above in terms of a non-dimensional length coordinate x/δ at selected air flow rates. Here x is the downstream distance measured from trailing edge of the porous section and δ denotes the undisturbed boundary-layer thickness at this location. These results are shown in figures 16 and 17. The figures have been reconstructed from mean lines drawn through C'_f/C'_{f0} versus Q_a data. Figure 16 compares the data for the plate above the boundary layer with that for the plate below the boundary layer data at $U_\infty = 16.8$ m/s. Figure 17 presents a similar comparison for $U_\infty = 10.8$ m/s. The persistence is clearly a function of the gravitational orientation and the tunnel velocity. The slope of the curves is steeper when

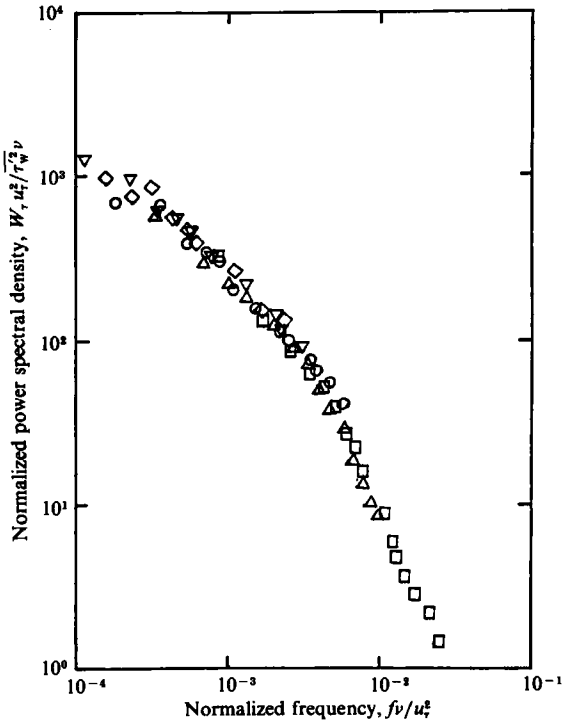

FIGURE 18. Normalized power-spectral-density functions of the hot-film signals in the absence of microbubbles (Probe 2; the plate on bottom): □, $U_\infty = 4.6$ m/s; △, 7.6 m/s; ○, 10.7 m/s; ▽, 13.8 m/s; ◇, 16.8 m/s.

the plate is below the boundary layer. At both velocities, the plate-on-bottom data showed that at low air flow rates the skin friction returns almost to its undisturbed value at the downstream probe location (roughly 35δ). At higher air flow rates, the skin-friction reductions with the plate on bottom are still significant at this location. Extrapolation of the plate-on-top data would indicate that the reductions persist even to 60–70 δ. This increased effectiveness is in keeping with other observations.

3.5. *Upstream effects due to introducing microbubbles in the flow*

In order to check for possible upstream effects of introducing microbubbles into the boundary layer, an additional hot film (probe 1) was mounted 10 mm upstream of the porous injection section. Skin-friction measurements at this location showed no change within the scatter of the data, when air was introduced. This verifies that the introduction of microbubbles into the flow is not felt upstream of the injection section over the range of velocities presented here.

3.6. *Comparison of hot-film and force-balance measurements*

The local skin-friction measurements from the array of hot films can be integrated and compared to the force-balance results reported in MDM1. The integrations were carried out using several different types of curve fits and integration procedures, all of which yielded quantitatively similar results (Madavan 1984). Excellent agreement was noted between the hot-film and the force-balance measurements. In all cases the maximum discrepancy between the two was less than 10 %. This agreement between two measurement techniques that are based on completely different physical principles provides substantiation for both.

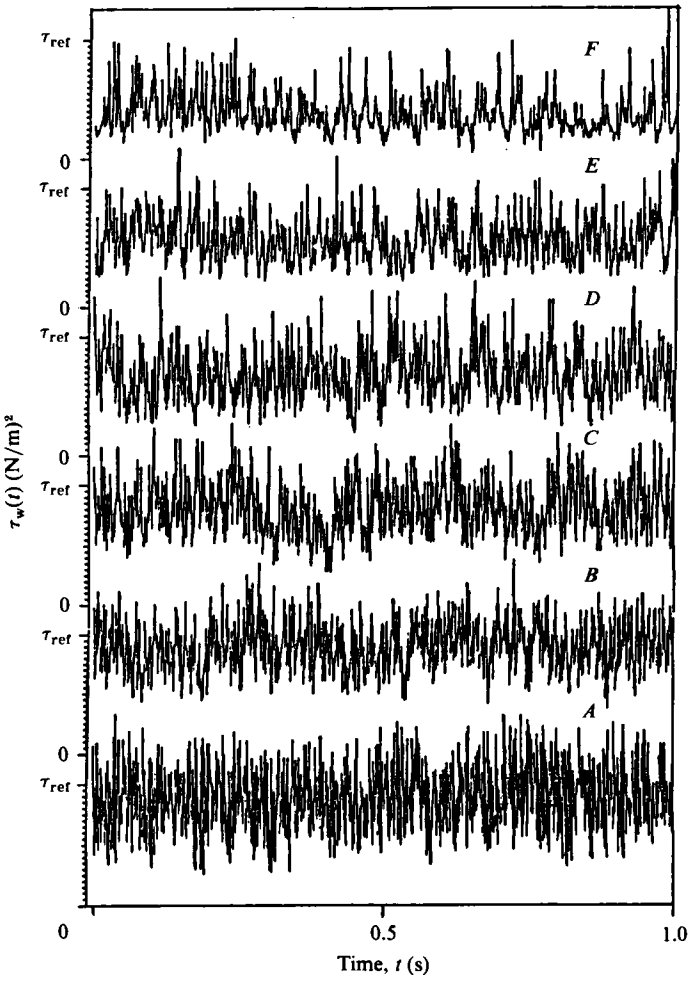

FIGURE 19. A sequence of linearized hot-film signal traces in the presence and absence of microbubbles (Probe 2; the plate on bottom): *A*, no microbubbles; *B*, 10% air, 5% C_f reduction; *C*, 14% air, 15% C_f reduction; *D*, 19% air, 28% C_f reduction; *E*, 26% air, 40% C_f reduction; *F*, 36% air, 62% C_f reduction.

3.7. *Spectral analysis of hot-film signals*

The effect of microbubbles on the near-wall turbulence structure was studied by extracting frequency information from the hot-film signals. A typical power-spectral-density function $W(f)$ defined by the equation

$$\tau'_w = \int_0^\infty W(f)\,df, \tag{5}$$

where f is the frequency in cycles per second, is presented in inner variables for no air injection in figure 18. The data is from probe 2 and the plate is on the bottom; the different symbols represent various velocities ranging between 4.0 and 17.0 m/s. The collapse of the data is quite good.

The influence of the microbubbles may be most strikingly observed by considering

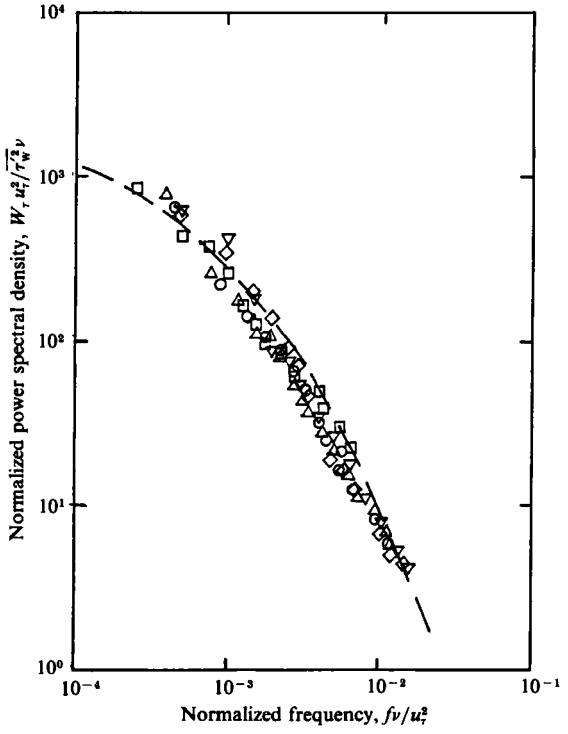

FIGURE 20. Normalized power-spectral-density functions of the hot-film signal in the presence of microbubbles. $U_\infty = 10.7$ m/s (Probe 2; the plate on bottom): —, $Q_a/(Q_a+Q_w) = 0$; □, 0.15; △, 0.30; ○, 0.35; ▽ and ⬡, 0.47.

a sequence of hot-film-signal traces comprising a typical run (probe 3, 16.8 m/s, plate on bottom) as shown in figure 19. The traces have been redrawn from the digitized, linearized signals as processed by the computer. The drop in the mean level of skin friction as the air flow rate is increased from zero is clearly seen with reference to a fixed skin-friction value, τ_{ref}. In the presence of microbubbles, the hot-film signals exhibit a reduced high-frequency content and the turbulence energy appears to shift toward lower frequencies.

In figures 20 and 21 the power-spectral-density functions with microbubbles for probe 2 at a free-stream speed of 10.7 m/s are shown in inner variables. Figure 20 is for the plate below the boundary layer while figure 21 is for the plate above. Note that u_τ and τ_w' used in these normalizations are the values with air injection, so that the loss of high-frequency signal is masked by the scaling. The inner-variable scaling thus remains effective for the microbubble boundary layer. Similar results are observed at higher speeds as shown in figure 22. These correspond to the signal traces previously presented in figure 19 (probe 3, 16.8 m/s, plate on bottom).

The power-spectral-density functions indicate, by the success of inner-variable scaling, that the introduction of air causes no major restructuring of the turbulent boundary layer. We note that there is a strong similarity between the results presented here and those obtained in the polymer flow of Fortuna & Hanratty (1972). Apparently there are some similarities in the drag reduction mechanisms for polymers and microbubbles.

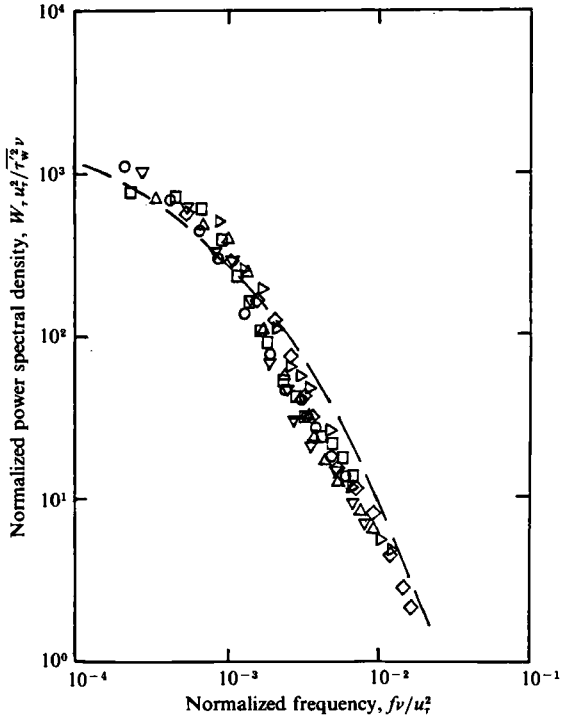

FIGURE 21. Normalized power-spectral-density functions of the hot-film signal in the presence of microbubbles. $U_\infty = 10.7$ m/s (Probe 2; the plate on top): --, $Q_a/(Q_a+Q_w) = 0$; □ and ○, 0.17; △, 0.24; ▽, 0.25; ◇, 0.27; ▷, 0.34.

4. Concluding remarks

An array of flush-mounted hot films has been used to study the downstream evolution and persistence of the skin-friction reduction in the microbubble-laden turbulent boundary layer. The measurements with the hot films are in excellent agreement with earlier reported integrated skin-friction measurements obtained using a force balance. The downstream persistence of the skin-friction reduction beyond the location of microbubble injection is a function of the gravitational orientation of the plate and the freestream velocity. For the plate above the boundary layer substantial skin-friction reductions persist for some 35δ for low air flow rates and up to 60–70 δ for high air flows. The reductions persist for somewhat shorter distances, roughly 50δ, for the plate below the boundary layer.

Contrary to earlier Soviet results, injection pore size was found to have no major effect on the amount of skin-friction reduction. A hot-film probe located 10 mm upstream of the porous injection section indicates that gas injection causes no significant upstream influence for the range of freestream speeds tested.

Spectral measurements indicate a clear loss of high-frequency signal with air injection. Inner-variable scaling of the spectra with u_τ and τ_w', however, seems as effective with microbubbles as without. This indicates that the major effect of the microbubbles in the turbulent boundary layer may be to alter the local effective viscosity and density of the fluid, thus changing the local turbulent Reynolds number, rather than introducing a major restructuring of the turbulence.

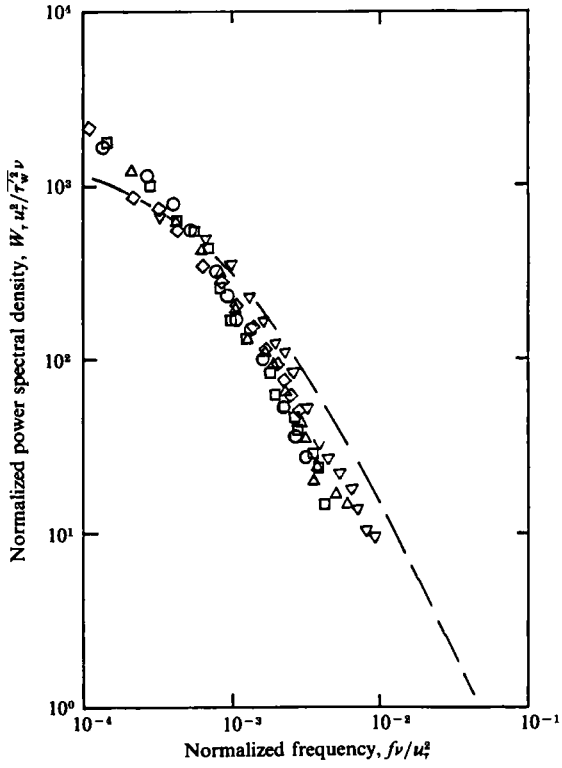

FIGURE 22. Normalized power-spectral-density functions of the hot-film signal in the presence of microbubbles. $U_\infty = 16.8$ m/s (Probe 3; the plate on bottom): ——, $Q_a/(Q_a+Q_w) = 0$; ◇, 0.10; ○, 0.14; □, 0.19; △, 0.26; ▽, 0.36.

This work was sponsored by the Office of Naval Research under Contract No. N00024-81-K-0481.

REFERENCES

BELLHOUSE, B. J. & SCHULTZ, D. L. 1966 Determination of mean and dynamic skin friction, separation and transition in low-speed flow with a thin-film heated element. *J. Fluid Mech.* **24**, 379.

BOGDEVICH, V. G. & EVSEEV, A. R. 1976 Effect of gas saturation on wall turbulence. In *Investigations of Boundary Layer Control* (in Russian) (eds. S. S. Kutateladze & G. S. Migirenko), p. 49. Thermophysics Institute Publishing House.

BOGDEVICH, V. G. & MALYAGA, A. G. 1976 The distribution of skin friction in a turbulent boundary layer of water beyond the location of gas injection. In *Investigations of Boundary Layer Control* (in Russian) (ed. S. S. Kutateladze & G. S. Migirenko), p. 62. Thermophysics Institute Publishing House.

BRADSHAW, P. & GREGORY, N. 1961 The determination of local turbulent skin friction from observations in the viscous sublayer. *Aero. Res. Counc. R & M* 3202.

BROWN, G. L. 1967 Theory and application of heated films for skin friction measurements. *Proc. 1967 Heat Transfer and Fluid Mech. Inst.* p. 361. Stanford University Press.

COLES, D. E. 1968 The young person's guide to the data. *Proc. AFOSR-IFP Stanford Conference on Computation of Turbulent Boundary Layers* (ed. D. E. Coles & E. A. Hirst). Stanford University Press.

ECKELMANN, H. 1974 The structure of the viscous sublayer and the adjacent wall region in a turbulent channel flow. *J. Fluid Mech.* **65**, 439.

FORTUNA, G. & HANRATTY, T. J. 1972 The influence of drag-reducing polymers on turbulence in the viscous sublayer. *J. Fluid Mech.* **53**, 575.

HANRATTY, T. J. & CAMPBELL, J. A. 1982 Measurement of wall shear stress. In *Fluid Mechanics Measurements* (ed. R. J. Goldstein). Hemisphere Publishing Corporation.

HUGHES, N. H., REISCHMANN, M. M. & HOLZMANN, J. M. 1979 Digital image analysis of two phase flow data. *6th Bienn. Symp. on Turbulence, University of Missouri, Rolla.*

LAUFER, J. 1950 Investigation of turbulent flow in a two dimensional channel. *NACA Rep. TN* 2123.

LIEPMANN, H. & SKINNER, G. 1954 Shearing-stress measurements by use of a heated element. *NACA TN* 3268.

MADAVAN, N. K. 1984 The effects of microbubbles on turbulent boundary layer skin friction. Ph.D. thesis, Dept. of Mech. Engng, The Pennsylvania State University.

MADAVAN, N. K., DEUTSCH, S. & MERKLE, C. L. 1984*a* Reduction of turbulent skin friction by microbubbles. *Phys. Fluids* **27**, 356.

MADAVAN, N. K., DEUTSCH, S. & MERKLE, C. L. 1984*b* The effect of porous material on microbubble skin friction reduction. *AIAA Paper* 84-0348.

MIGIRENKO, G. S. & EVSEEV, A. R. 1974 Turbulent boundary layer with gas saturation. In *Problems of Thermophysics and Physical Hydrodynamics* (in Russian). Novosibirsk, Nauka.

MITCHELL, J. E. & HANRATTY, T. J. 1966 A study of turbulence at a wall using an electrochemical wall shear stress meter. *J. Fluid Mech.* **26**, 199.

PURTELL, L. P., KLEBANOFF, P. S. & BUCKLEY, F. T. 1981 Turbulent boundary layer at low Reynolds number. *Phys. Fluids* **24**, 802.

RAMAPRIAN, B. R. & TU, S. W. 1983 Calibration of a heat flux gage for skin friction measurement. *Trans. ASME* I: *J. Fluids Engng* **104**, 455.

SANDBORN, V. A. 1979*a* Surface shear stress fluctuations in turbulent boundary layers. *Second Symp. on Turbulent Shear Flows, Imperial College, London*, p. 361.

SANDBORN, V. A. 1979*b* Evaluation of the time dependent surface shear stress in turbulent flows. *ASME Preprint* 79-WA/FE-17.

SILBERMAN, E. 1957 Production of bubbles by the disintegration of gas jets in liquid. In *Proc. 5th Midwestern Conf. on Fluid Mech., University of Michigan*, p. 263.

SIRKAR, K. K. & HANRATTY, T. J. 1970 The limiting behaviour of the turbulent transverse velocity component close to a wall. *J. Fluid Mech.* **44**, 589.

WHITE, F. M. 1974 *Viscous Fluid Flow.* McGraw-Hill Publishing Co.